This is a post-peer-review, pre-copyedit version of an article published in Soil Dynamics and Earthquake Engineering. The final authenticated version is available online at: http://dx.doi.org/10.1016/j.soildyn.2019.02.015

TITLE:

EFFECTS OF COSEISMIC GROUND VERTICAL MOTION ON MASONRY CONSTRUCTIONS DAMAGE DURING THE 2016 AMATRICE-NORCIA (CENTRAL ITALY) EARTHQUAKES

AUTHORS:

Liberatore D[a*], Doglioni C[b,c], AlShawa O[a], Atzori S[b], Sorrentino L[a]

[a] Department of Structural and Geotechnical Engineering, “Sapienza” University of Rome, Rome, Italy

[b] Istituto Nazionale di Geofisica e Vulcanologia, Rome, Italy

[c] Department of Earth Sciences, “Sapienza” University of Rome, Rome, Italy

*corresponding author

ORCID

Liberatore D: 0000-0003-3184-8189; Doglioni C: 0000-0002-8651-6387; AlShawa O: 0000-0001-7905-5482; Atzori S: 0000-0002-5031-9904; Sorrentino L: 0000-0003-1652-942X.

ABSTRACT

Horizontal acceleration and velocity are considered the most important parameters in determining damage potential to buildings during the paroxysmal energy dissipation of an earthquake. However, taking as example the two mainshocks of the 2016 Central Italy seismic sequence and comparing Interferometric Synthetic-Aperture Radar (InSAR) and macroseismic data, it is shown that maximum damage was concentrated where the ground subsided coseismically. A number of empirical relationships are determined between InSAR vertical displacement on the one hand, and macroseismic intensity or ground motion intensity measures on the other. Finally, resorting to a finite-discrete element model, the effect of the vertical component of ground motion is investigated on a test masonry structure under recorded accelerograms.

KEYWORDS:
InSAR; macroseismic intensity; intensity measures; finite-discrete element.

1 INTRODUCTION

In 2016, Central Italy was struck by a seismic sequence consisting of two mainshocks, M_w 6.0 on August 24th and M_w 6.5 on October 30th (Chiaraluce et al. 2017). The seismicity was generated by the tectonic extensional stress regime affecting the Apennines ridge (Bigi et al., 1989, Petricca et al. 2015, Doglioni et al. 2015), where a rate of around N50°E dilation of about 4-5 mm/yr is recorded through permanent GPS networks (Devoti et al. 2017) across the belt from the Tyrrhenian coast to the highest peaks, which are on average slightly east of the water divide. A large number of multidisciplinary data were collected during the sequence, namely seismological, geological, geodetic (GPS and Interferometric Synthetic-Aperture Radar (InSAR)), strong motion and macroseismic surveys (Cheloni et al. 2017, Wilkinson et al. 2017, Azzaro et al. 2016, Tertulliani and Azzaro 2016). This research was motivated by the overlap between the most damaged areas and the coseismically subsided zone. The concentration of damage can be explained locally by site-amplification effects and seismic wave directivity (Azzaro et al. 2016, Calderoni et al. 2017). However, a further effect could be provided by the combination of the horizontal components of ground motion and the simultaneous vertical acceleration (Ganz and Doglioni 2014, Mariani and Pugi 2018). In this study, InSAR vertical displacement is compared with macroseismic data and ground motion intensity in order to explain the greater destruction of masonry buildings in the coseismically subsided area (Figures 1-2). In Figure 2, macroseismic data also cumulate the effects of the previous M_w 6.0 August 24 earthquake. It is evident from interferometric data that the area struck by the earthquake is divided into two coseismically deformed areas, i.e., subsided and uplifted. The subsided area is much more pronounced than them part that was uplifted, and macroseismic data point to more severe damage within the subsided area. In fact, the most severe damage is concentrated in the area that underwent subsidence, whereas settlements closer to the epicentre, but coseismically uplifted, experienced less destruction.

This study investigates the influence of combined horizontal and vertical components (Figure 3) on the dynamic nonlinear response of unreinforced masonry structures. Downward (upward) acceleration entails instantaneous decrement (increment) of friction force and corresponding potential

This is a post-peer-review, pre-copyedit version of an article published in Soil Dynamics and Earthquake Engineering. The final authenticated version is available online at: http://dx.doi.org/10.1016/j.soildyn.2019.02.015

increment (decrement) of sliding between the bricks or stones of masonry buildings, depending on the level of horizontal action at the same instant.

This article focuses on this observation, investigating numerically the dynamic effect of the variation of friction forces between units and mortar induced by vertical acceleration.

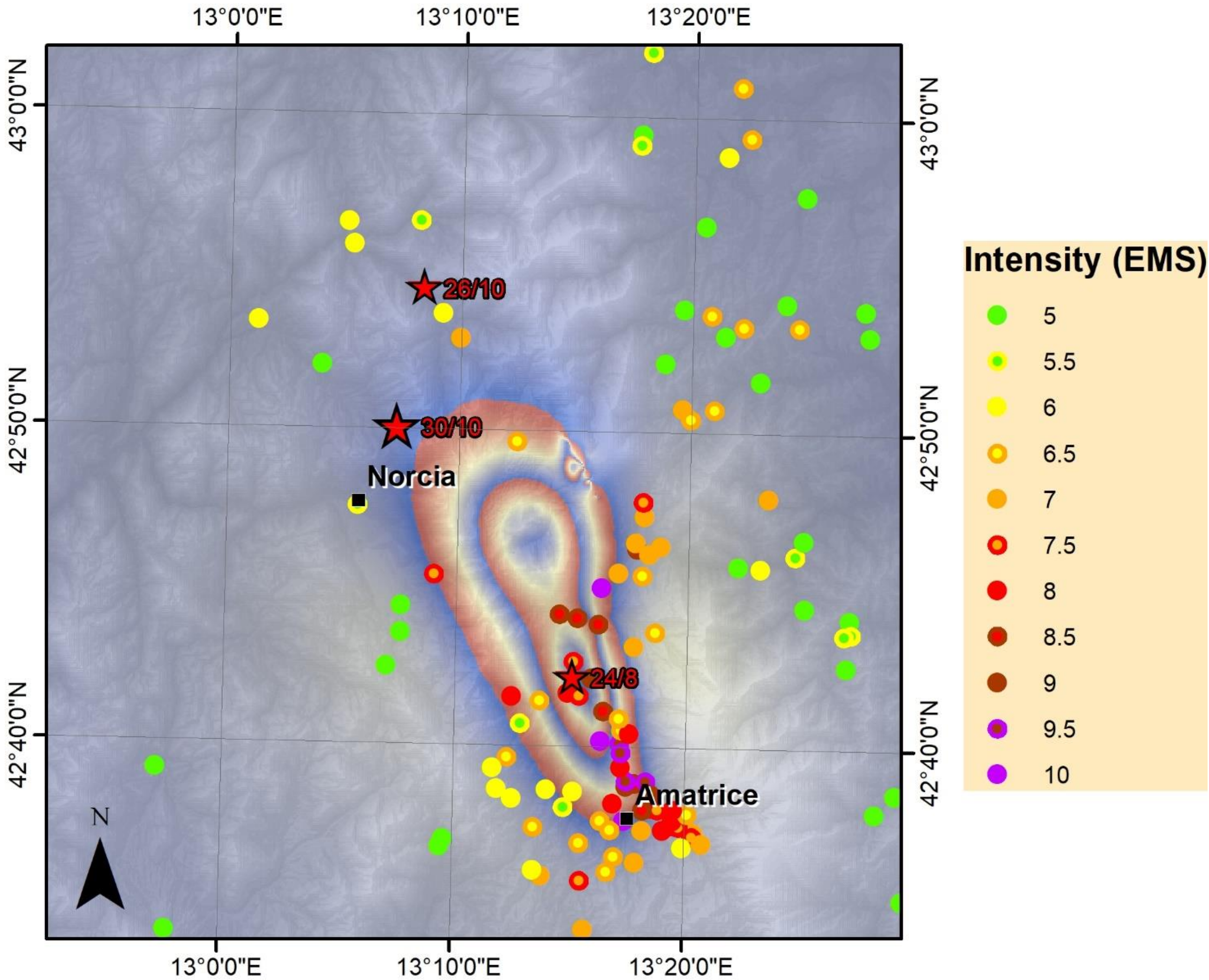

Figure 1. InSAR coseismic subsidence (max ~200 mm) and macroseismic data associated with the M_w 6.0 August 24th 2016 mainshock. The vertical displacement field has been rewrapped so that each fringe corresponds to 100 mm.

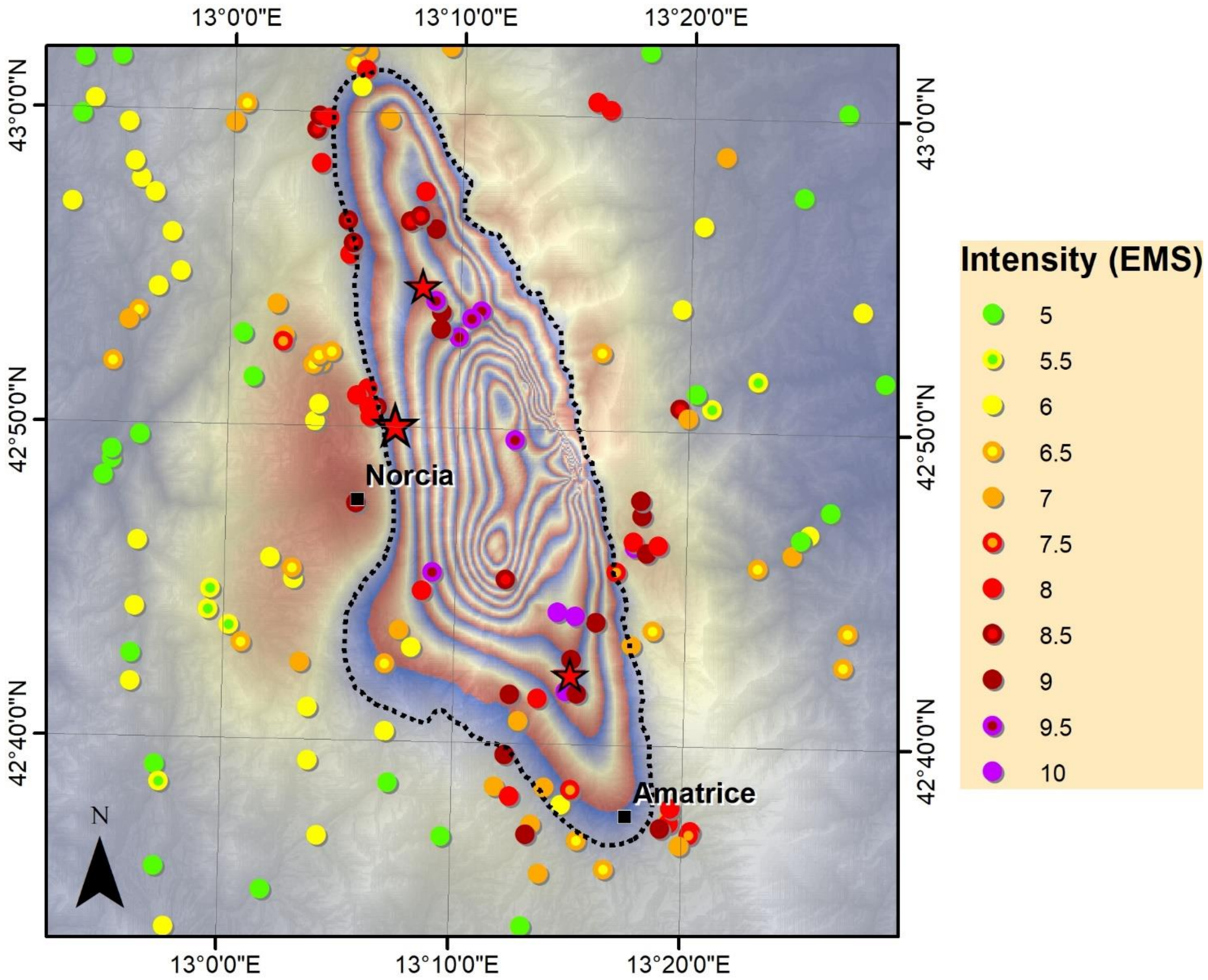

Figure 2. InSAR coseismic subsidence (max ~1000 mm east of Norcia) and macroseismic data associated with the M_w 6.5 October 30th 2016 mainshock. The vertical displacement field has been rewrapped so that each fringe corresponds to 100 mm.

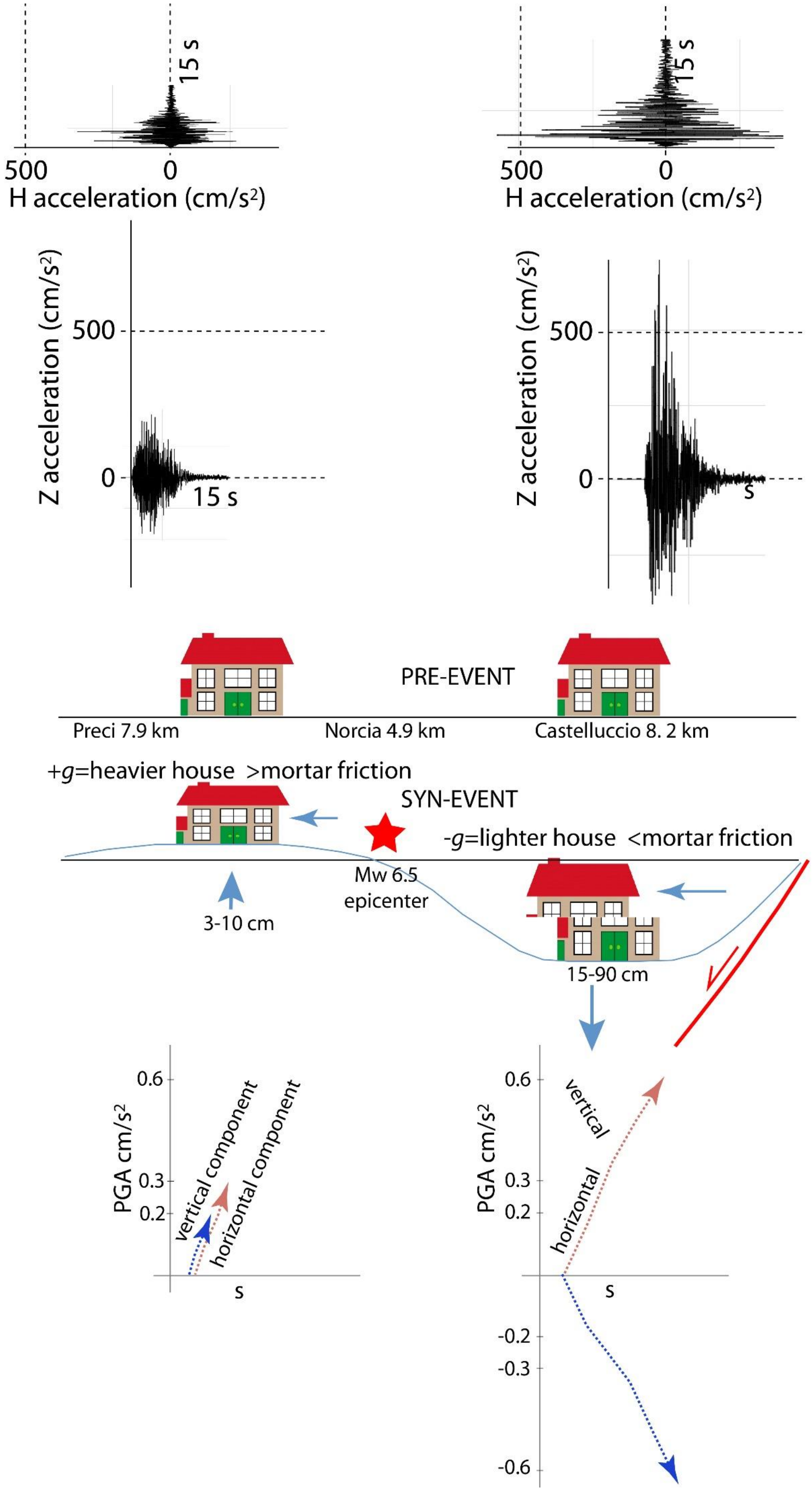
15 s
500
0
H acceleration (cm/s2)
15 s
500
0
H acceleration (cm/s2)
Z acceleration (cm/s2)
500
0
15 s
Z acceleration (cm/s2)
500
0
s
PRE-EVENT
Preci 7.9 km
Norcia 4.9 km
Castelluccio 8. 2 km
+g=heavier house >mortar friction
SYN-EVENT
-g=lighter house <mortar friction
Mw 6.5
epicenter
3-10 cm
15-90 cm
PGA cm/s2
0.6
0.3
0.2
vertical component
horizontal component
s
PGA cm/s2
0.6
0.3
0.2
-0.2
-0.3
-0.6
vertical
horizontal
s

Figure 3. Model investigated in this study. Higher panels: Ground motion components occurring at the same time. Lower panels: A short fraction of an accelerogram, with acceleration versus time (s) showing two cases in which the coseismic motion is upward (left) or downward (right) during the increase of horizontal components.

2 InSAR DATA

Displacement data used in this analysis are derived from InSAR measurements. InSAR processing is, nowadays, one of the most commonly used techniques to depict the spatial distribution of the permanent displacement occurred after a seismic event (see Weston et al. 2011 and references therein). This technique is based on radar phase comparison of two SAR images acquired with the same satellite, at the same orbit and at the same position, but at two distinct times, before and after the event (Franceschetti and Lanari 1999).

Though the description of the InSAR rationale is beyond the goal of this work, it is worth noting that the displacement measurements obtained from the radar phase difference are in the Line-of-Sight (LoS) direction, i.e. a diagonal line connecting the satellite to the pixel on the ground, nearly East-West and tilted ~40° from the vertical (this angle has a rather wide range of values, according to the satellite). This peculiar SAR geometry makes the rigorous derivation of horizontal and vertical displacement components complex; in order to bypass the unavoidable approximations affecting every approach based only on the combination of different LoSs, the vertical displacement is derived from the Central Italy source models shown in Cheloni et al. (2017).

At the basis of this approach is analytical source modelling, whose rationale is described in Atzori et al. (2009): an exhaustive dataset of InSAR maps is handled by means of linear and non-linear inversion optimizations to derive the seismic sources responsible for the permanent displacement of both events. These sources are then used as input for forward modelling to get the estimated displacement along the East, North and vertical directions, the latter being the one used in this work. This model-based approach to get a complete 3D displacement has the further advantage of filtering out most of the atmospheric artifacts that generally affect InSAR maps and cannot be *a priori* discriminated from the real displacement signal. In fact, atmospheric artifacts are almost impossible to fit within the modelling optimization and are therefore absent in the forward calculation.

In addition to InSAR data used to get the source models for the August 24 and October 30 earthquakes, and reported in Table 1, GPS data from the Ca.Geo.Net. network (Galvani et al. 2012) and the Italian Istituto Geografico Militare network were also considered.

Table 1. SAR image acquisitions.

SAR images		**Satellite/ Constellation**	**Space Agency**	**Orbit**	**Radar band**
pre-event	**post-event**				
August, 24 event					
August, 20	August, 28	COSMO-SkyMed	Italian (ASI)	ascending	X-band
August, 20	August, 26	COSMO-SkyMed	Italian (ASI)	descending	X-band
August, 21	August, 27	Sentinel-1	European (ESA)	ascending	C-band
August, 21	August, 27	Sentinel-1	European (ESA)	descending	C-band
September, 15*	August, 24	ALOS-2	Japanese (JAXA)	ascending	L-band
May, 25	August, 31	ALOS-2	Japanese (JAXA)	descending	L-band
October, 30 event**					
September, 9*	November, 2	ALOS-2	Japanese (JAXA)	ascending	L-band
May, 25	November, 9	ALOS-2	Japanese (JAXA)	descending	L-band

* 2015

** Both pairs include the effects of the August 24th event.

3 RELATIONSHIPS BETWEEN InSAR VERTICAL DISPLACEMENT AND MACROSEISMIC INTENSITY

A first group of empirical relationships between InSAR vertical displacement and macroseismic intensity was investigated for the 2016 August 24 mainshock. Concerning the following events, although InSAR displacement was somewhere higher, like the one on the October 30, 2016, the determination of these relationships is more problematic because of cumulated intensity.

The Mercalli-Cancani-Sieberg (MCS) intensities, I_{MCS} (Galli et al. 2016) and the European Macroseismic Scale (EMS) intensities, I_{EMS} (Azzaro et al. 2016) are reported in Table 2 for the sites with I_{MCS}, $I_{EMS} \geq$ VI, with the corresponding modelled InSAR vertical displacements, denoted by w.

Table 2. I_{MCS}, I_{EMS} vs. InSAR vertical displacement w, August 24th, 2016 mainshock (I_{MCS}, $I_{EMS} \geq$ VI).

Site	**Municipality and Province abbreviation**	I_{MCS}	I_{EMS}	w **(m)**

Amatrice	Amatrice RI	X-XI	X	–0.0464
Petrana	Amatrice RI	X-XI	IX-X	–0.0819
Pescara del Tronto	Arquata del Tronto AP	X-XI	X	–0.0764
Illica	Accumoli RI	X	IX-X	–0.1984
Casale	Amatrice RI	X	IX-X	–0.0948
Saletta	Amatrice RI	X	X	–0.1492
Rio	Amatrice RI	IX-X		–0.0870
San Lorenzo e Flaviano	Amatrice RI	IX-X	IX-X	–0.0947
Sant'Angelo	Amatrice RI	IX-X	IX-X	–0.0468
Faizzone	Amatrice RI	IX		–0.0635
Sommati	Amatrice RI	IX	IX	–0.0301
Crognale	Amatrice RI		IX	–0.0790
Accumoli	Accumoli RI	VIII-IX	VIII	–0.1740
Grisciano	Accumoli RI	VIII-IX	VIII-IX	–0.0953
Poggio Casoli	Accumoli RI	VIII-IX	VIII-IX	–0.1651
Cornillo Vecchio	Amatrice RI	VIII-IX	VIII	–0.0689
Cossito	Amatrice RI	VIII-IX	VIII	–0.0564
Retrosi	Amatrice RI	VIII-IX	VIII	–0.0175
Rocchetta	Amatrice RI	VIII-IX	VIII	–0.0959
Arquata del Tronto	Arquata del Tronto AP	VIII-IX	VIII-IX	0.0027
Capodacqua	Arquata del Tronto AP	VIII-IX	VIII-IX	–0.1672
Tufo	Arquata del Tronto AP	VIII-IX	VIII-IX	–0.1557
Fonte del Campo	Accumoli RI	VIII	VII-VIII	–0.2148
Cascello	Amatrice RI	VIII	VII-VIII	–0.0325
Moletano	Amatrice RI	VIII	VIII	–0.0155
Santo Masso	Amatrice RI	VIII		–0.0930
San Giovanni	Accumoli RI	VII-VIII	VIII	–0.0388
Tino	Accumoli RI	VII-VIII	VII-VIII	–0.2043
Collepagliuca	Amatrice RI	VII-VIII	VII-VIII	–0.0254
Prato	Amatrice RI	VII-VIII	VIII-IX	–0.0478
San Capone	Amatrice RI	VII-VIII		–0.0777
Pretare	Arquata del Tronto AP	VII-VIII	VII-VIII	0.0037
Cossara	Amatrice RI		VII-VIII	–0.0144
Fornisco	Valle Castellana TE		VII-VIII	0.0017
Villanova	Accumoli RI	VII	VI-VII	–0.0865
Capricchia	Amatrice RI	VII	VII	0.0090
Poggio Vitellino	Amatrice RI	VII		–0.0964

San Lorenzo a Pinaco	Amatrice RI	VII		–0.0081
Scai	Amatrice RI	VII	VII	0.0050
Torrita	Amatrice RI	VII		0.0031
Voceto	Amatrice RI	VII	VIII	0.0012
Borgo	Arquata del Tronto AP	VII	VII	0.0015
Faete	Arquata del Tronto AP	VII		0.0088
Piedilama	Arquata del Tronto AP	VII	VII	0.0041
Trisungo	Arquata del Tronto AP	VII	VII	0.0106
Castro	Montegallo AP	VII	VII	0.0042
San Pellegrino	Norcia PG	VII	VII-VIII	–0.0213
Faete	Arquata del Tronto AP		VII	0.0087
Poggio d’Api	Accumoli RI		VII	0.0054
Santa Lucia	Montereale AQ		VII	0.0043
Tallacano	Acquasanta Terme AP		VII	0.0049
Vezzano	Arquata del Tronto AP		VII	–0.0109
Colleposta	Accumoli RI	VI-VII	VI-VII	–0.0075
Falciano	Acquasanta Terme AP	VI-VII		0.0030
Arafranco-Pinaco	Amatrice RI	VI-VII	VII	–0.0039
Castel Trione	Amatrice RI	VI-VII	VII-VIII	0.0082
Cornelle di Sotto	Amatrice RI	VI-VII	VII-VIII	0.0019
Ferrazza	Amatrice RI	VI-VII	VII-VIII	–0.0045
Mosicchio	Amatrice RI	VI-VII	VI-VII	–0.0307
Preta	Amatrice RI	VI-VII	VII	0.0080
San Benedetto	Amatrice RI	VI-VII		–0.0298
San Cipriano	Amatrice RI	VI-VII	VII	–0.0182
Santa Giusta	Amatrice RI	VI-VII	VI	–0.0466
Spelonga	Arquata del Tronto AP	VI-VII	VI-VII	0.0041
Balzo	Montegallo AP	VI-VII	VI-VII	0.0044
Castelluccio	Norcia PG		VI-VII	–0.0607
Collalto	Amatrice RI		VI-VII	–0.0825
Colle	Arquata del Tronto AP		VI-VII	0.0182
Collecreta	Amatrice RI		VI-VII	–0.0112
Configno	Amatrice RI		VI-VII	–0.0100
Nommisci	Amatrice RI		VI-VII	–0.0026
Collegentilesco	Amatrice RI	VI	VI-VII	0.0000
Collemoresco	Amatrice RI	VI	VI	–0.0195
Colli	Amatrice RI	VI	VI-VII	–0.0397
Cornillo Nuovo	Amatrice RI	VI	VI	0.0054

Pasciano	Amatrice RI	VI	VI	0.0012
Castelsantangelo sul Nera	Castelsantangelo sul Nera MC	VI	VI	–0.0017
Gualdo	Castelsantangelo sul Nera MC	VI	VII	–0.0047
Nocria	Castelsantangelo sul Nera MC	VI		–0.0010
Norcia	Norcia PG	VI		0.0006
Nottoria	Norcia PG	VI		–0.0072
Ceraso	Valle Castellana TE	VI		0.0020
Morrice	Valle Castellana TE	VI		0.0034
Forcelle	Amatrice RI		VI	0.0031
Pascellata	Valle Castellana TE		VI	0.0021
Quintodecimo	Acquasanta Terme AP		VI	0.0069
Roccasalli	Accumoli RI		VI	0.0012
Varoni	Amatrice RI		VI	0.0049

AP: Ascoli Piceno, AQ: L'Aquila, MC: Macerata, PG: Perugia, RI: Rieti, TE: Teramo.

The sites with maximum InSAR downward displacement were Fonte del Campo, Tino and Illica, all located in the Municipality of Accumoli, with vertical displacement around –0.20 m.
The regression of InSAR vertical displacement and MCS intensity is reported in Figure 4 (R^2 = 0.4631):

$$w = -0.0215\, I_{MCS} + 0.1133 \qquad (\, w \text{ in m}) \tag{1}$$

The regression was determined by also considering intensities V ≤ I_{MCS} < V-VI. The higher the downward displacement, the higher the MCS intensity.
It can be observed that downward displacement for the centre of Amatrice is moderate (w = –0.04643 m) but MCS intensity reaches its highest value (I_{MCS} = X-XI). Topographic amplification related to crest morphology and severe damage induced by poor masonry quality (Sorrentino et al. 2018) are possible explanations. On the other hand, MCS intensities for sites such as Tino and Fonte del Campo, both in the Municipality of Accumoli, with greatest downward displacement, were moderate, namely VII-VIII and VIII, respectively. Similarly, downward displacement for the site of Forche Canepine, in the Municipality of Arquata del Tronto, was high (w = –0.14625 m) with low intensity (I_{MCS} = V). However, this site has few buildings, possibly resulting in a non-robust estimation of intensity.
Inverse regression, i.e. calculating the errors along the direction of the I_{MCS} axis, is:

$$I_{MCS} = -21.52\, w + 5.714 \qquad (w \text{ in m}) \tag{2}$$

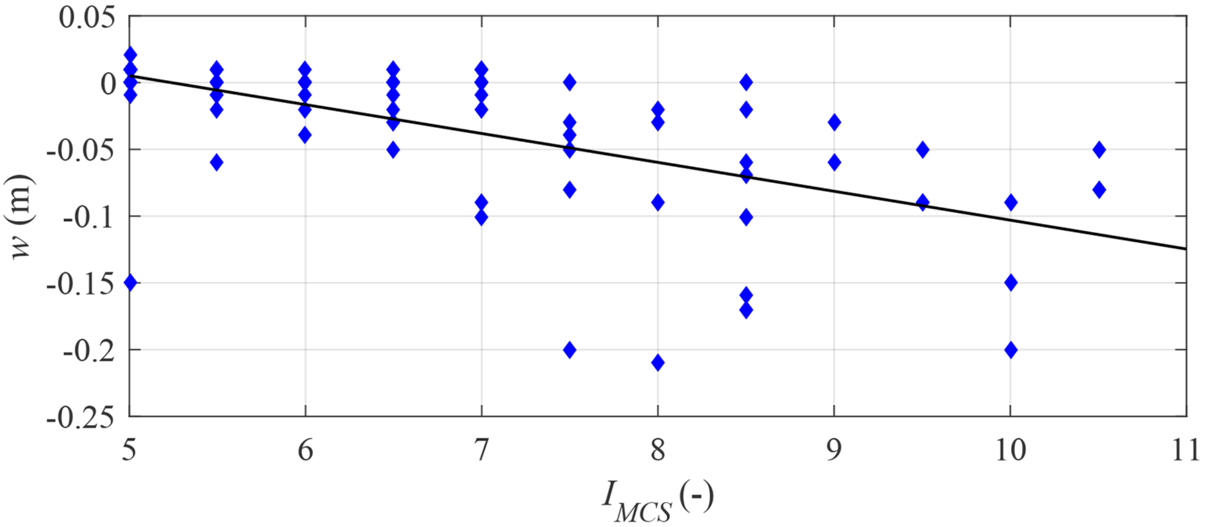

Figure 4. Regression between InSAR vertical displacement and MCS intensity (Eq. (1)).

Similar regressions were derived for EMS intensity (Figure 5), but with larger scatter (R^2 = 0.3711):

$$w = -0.0214\, I_{EMS} + 0.1169 \qquad (w \text{ in m}) \tag{3}$$

$$I_{EMS} = -17.32\, w + 6.134 \qquad (w \text{ in m}) \tag{4}$$

It can be observed that the regressions w-I_{MCS} and w-I_{EMS} are almost coincident, whereas the inverse regressions show significant differences.

The inverse regressions (Eqs. 2,4) provide an estimation of MCS and EMS intensity, respectively, given the InSAR data. However, it must be emphasised that further studies on a statistically significant set of earthquakes are needed to systematically exploit InSAR data for a quick estimate of macroseismic intensities in the aftermath of an event.

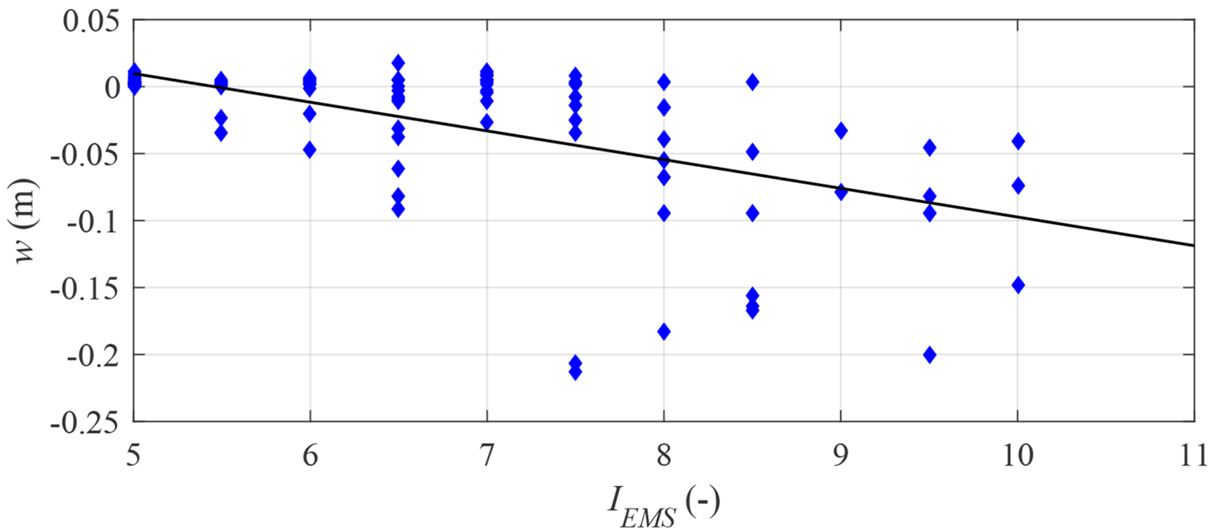

Figure 5. Regression between InSAR vertical displacement and EMS intensity (Eq. (3)).

A comparison of MCS and EMS intensities is also interesting. Taking into account only intensity values greater than or equal to VI, the I_{EMS}-I_{MCS} regression is (R^2 = 0.8569):

$$I_{EMS} = 0.7302\, I_{MCS} + 2.173 \qquad (5)$$

resulting in almost equal values for I_{MCS} = VIII ≅ I_{EMS}, whereas for I_{MCS} = VI, I_{EMS} ≅ VI-VII, and for I_{MCS} = X, I_{EMS} ≅ IX-X. The inverse regression is:

$$I_{MCS} = 1.174\, I_{EMS} - 1.472 \qquad (6)$$

It is worth noting that this relationship differs in terms of constant value from the relationship proposed by Margottini et al. (1987): $I_{MCS} = 1.17\, I_{EMS} - 0.76$.

4 RELATIONSHIPS BETWEEN InSAR VERTICAL DISPLACEMENT AND GROUND MOTION INTENSITY MEASURES

A second group of empirical relationships links InSAR vertical displacement to horizontal ground motion intensity measures. These parameters, in turn, can be related to macroseismic intensity by means of empirical relationships established in literature. Ground motion intensity measures, as opposed to macroseismic intensities, are continuous quantities, are not affected by the intrinsic scatter related to structural response, and are not affected by the conventional estimation of damage and vulnerability, and by damage accumulation. On the other hand, the number of records in sites experiencing downward displacements is rather limited. For the mainshock of August 24, 2016, just one station (Amatrice) is available and, for the shock of October 30, 2016, five stations, thanks also to the mobile accelerometric network (Luzi et al. 2017). InSAR data for October 30th cumulate the effects of the shocks of October 26th and 30th.

For the 2016 October 30 event, it can also be observed that, for a given distance from the epicentre, greater vertical acceleration was recorded in zones with downward displacement than in uplifted areas.

Different ground motion intensity measures are considered, calculated from corrected horizontal accelerograms. Peak ground acceleration (*PGA*) and peak ground velocity (*PGV*) are selected as ground motion parameters because they are the most commonly used intensity measures. The ratio between peak ground acceleration and peak ground velocity (*PGA*/*PGV*) provides useful information on frequency content, and is inversely correlated with magnitude, duration, epicentral distance and the predominant period of the site (Castaldo and Tubaldi 2018). The *PGA*/*PGV* ratio is expressed in the form PGA / (g PGV), where g is the gravitational acceleration. Dimensionally, the ratio PGA / (g PGV) is the inverse of a velocity.

Another velocity measure is maximum incremental velocity (*IV*), given by the area below the largest acceleration pulse (Anderson and Bertero 1987). Peak ground displacement (*PGD*) is not considered in this study because of the correction procedure consisting of baseline correction, non-causal 2nd order high-pass and low-pass Butterworth filter, cosinusoidal taper and removal of linear displacement drift (Luzi et al. 2017). The effect of this procedure is a zero final displacement, which contrasts with physical evidence and InSAR data. A further confirmation of non-zero final displacement is provided by high frequency GPS records (Wilkinson et al. 2017).

Among instrumental intensity measures, Arias, Fajfar and Housner Intensities are taken into consideration. Arias Intensity (I_A) (Arias 1970) is given by:

$$I_A = \frac{\pi}{2g}\int_0^\infty a_g^2(t)dt \tag{7}$$

where a_g is ground acceleration and t time. Arias Intensity has been proved to represent the sum of the total energies, per unit weight, stored at the end of the earthquake ground motion in a population of undamped linear oscillators. Arias Intensity, which dimensionally is a velocity, can be correlated to damage (Cabañas et al. 1997) but tends to overestimate the intensity of earthquakes with long duration, high acceleration and broad band frequency content (Uang and Bertero 1988). Arias

Intensity has been demonstrated to be an effective predictor of damage to short-period structures (Stafford et al. 2009).

Fajfar Intensity (I_F) (Fajfar et al. 1990) is defined as:

$$I_F = PGV\ t_D{}^{0.25} \tag{8}$$

where centimetres and seconds are used, t_D is the Trifunac and Brady strong motion duration (Trifunac and Brady 1975):

$$t_D = t_{0.95} - t_{0.05} \tag{9}$$

and $t_{0.05}$ and $t_{0.95}$ are the time values at which 5% and 95% of the time integral of the history of squared accelerations are reached, respectively. Fajfar Intensity was formulated to represent earthquake potential to damage medium-period structures.

Housner Intensity (I_H) (Housner 1952) is defined as the integral of the elastic pseudo-velocity spectrum, over the period T ranging between 0.1 and 2.5 s:

$$I_H = \int_{0.1}^{2.5} S_{pv}(T, \xi = 0.05)dT = \frac{1}{2\pi}\int_{0.1}^{2.5} S_{pa}(T, \xi = 0.05)TdT \tag{10}$$

where S_{pv} and S_{pa} are the pseudo-velocity and the pseudo-acceleration, respectively, at undamped natural period T and damping ratio $\xi = 0.05$. Dimensionally, Housner Intensity is a displacement. Housner Intensity can be considered as the first moment of the area of S_{pa} (0.1 s ≤ T ≤ 2.5 s) about the S_{pa} axis. Therefore, it is larger for ground motions with a significant amount of low frequency content.

The analysis has been carried out taking into account the record at Amatrice of August 24, 2016, and the five records of October 30, 2016, (Luzi et al. 2017) in the zone of downward displacement ($w \leq -10$ mm).

A set of directions in the horizontal plane, with angular step 10°, has been considered, the aim being to determine the highest values of horizontal ground motion intensity measures. For each direction, acceleration time history has been calculated by projecting the NS and EW components, and ground motion intensity measures have been determined. The maximum values of the parameters are reported in Table 3.

Table 3. Ground motion intensity measures in the downward displacement zone.

Station	**Date**	M_w	**Soil type**	**Epicentral distance (km)**	PGA (cm/s^2)	PGV (cm/s)	PGA / (g PGV) (s/m)	IV (cm/s)	I_A (cm/s)	I_F (cm s$^{-3/4}$)	I_H (cm)	w (m)
AMT	2016/08/24	6.0	B	8.5	851.2	45.18	1.921	79.40	188.2	62.85	121.2	−0.056
CLO	2016/10/30	6.5	A*	7.8	590.5	69.58	0.865	123.31	443.9	117.25	277.4	−0.780
CNE	2016/10/30	6.5	C*	7.7	487.2	41.66	1.192	70.71	197.4	64.92	129.8	−0.198
FCC	2016/10/30	6.5	A*	11.0	938.5	81.76	1.170	139.01	840.2	127.20	233.3	−0.455
IV.T1213	2016/10/30	6.5	A*	12.0	883.5	62.03	1.452	89.48	616.1	99.76	158.7	−0.085
IV.T1214	2016/10/30	6.5	B*	11.4	623.7	56.24	1.130	59.43	399.2	90.70	143.8	−0.426

The regressions of PGA, PGV, PGA / (g PGV), IV, I_A, I_F, I_H vs. w are:

$$PGA = 225.0w + 804.1 \qquad (PGA \text{ in cm/s}^2, w \text{ in m}) \qquad (R^2 = 0.1124) \tag{11}$$

$$PGV = -33.35\, w + 48.30 \qquad (PGV \text{ in cm/s}, w \text{ in m}) \qquad (R^2 = 0.3720) \tag{12}$$

$$PGA/(g\, PGV) = 1.108\, w + 1.658 \quad (PGA/(g\, PGV) \text{ in s/m}, w \text{ in m}) \quad (R^2 = 0.7138) \tag{13}$$

$$IV = -62.38\, w + 72.77 \qquad (IV \text{ in cm/s}, w \text{ in m}) \qquad (R^2 = 0.3050) \tag{14}$$

$$I_A = -278.4\, w + 354.7 \qquad (I_A \text{ in cm/s}, w \text{ in m}) \qquad (R^2 = 0.0937) \tag{15}$$

$$I_F = -66.50\, w + 71.62 \qquad \left(I_F \text{ in cm/s}^{-3/4}, w \text{ in m}\right) \qquad (R^2 = 0.4804) \tag{16}$$

$$I_H = -197.4\, w + 111.6 \qquad (I_H \text{ in cm}, w \text{ in m}) \qquad (R^2 = 0.7406) \tag{17}$$

The regressions only hold in the downward displacement zone ($w \le -10$ mm) and cannot be extended to the upward or negligible vertical displacement zones. They provide a preliminary indication of the relationship between InSAR vertical displacement and ground motion intensity measures.

It can be observed that the correlation of InSAR displacement with the parameters related to high frequency content (PGA, I_A) is limited. It can also be observed that PGA is positively correlated with w, and this further confirms the limited reliability of the PGA-w regression.

InSAR vertical displacements are moderately correlated with the parameters related to intermediate frequency content (PGV, IV, I_F), and well correlated with the ratio PGA / (g PGV) and Housner Intensity I_H, (Figure 6), the latter being mainly related to low frequency content. Regarding Housner Intensity, studies in literature (Decanini et al. 2002, Masi et al. 2011, Marotta et al. 2017) demonstrated that it can be a valid alternative to other seismic peak parameters, and in (Chiauzzi et al. 2012) a relationship between Housner Intensity and EMS intensity was developed.

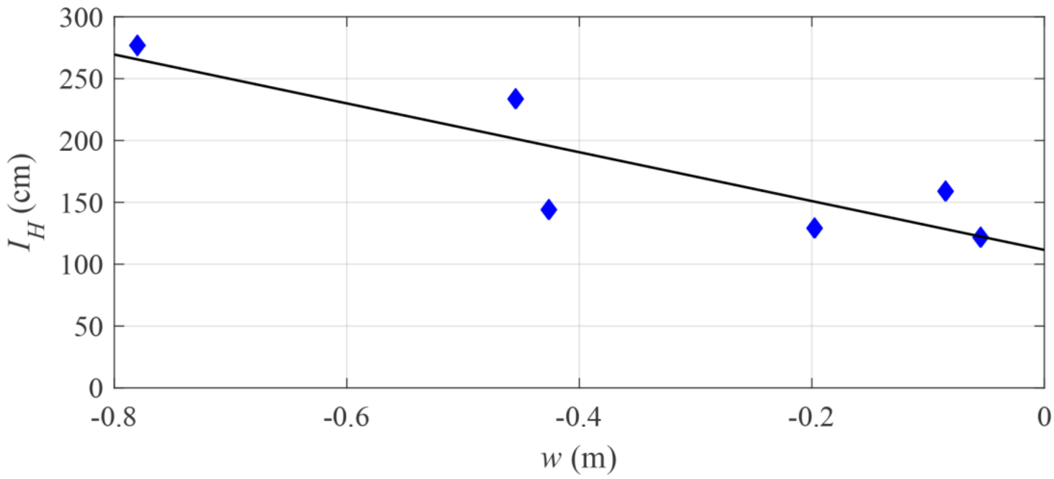

Figure 6. Regression between Housner Intensity and InSAR vertical displacement.

5 EFFECT OF THE VERTICAL COMPONENT ON THE SEISMIC RESPONSE OF A MASONRY TEST STRUCTURE

The effect of the vertical component on the seismic response of a masonry structure has been investigated by means of numerical simulations of the response of a test structure in natural stone shown in Figure 7. The façade is 4.15 m in width and reaches a maximum height of 3.00 m; the lateral walls are 2.50 m wide and 2.45 m high. Thickness for both façade and lateral walls is 0.50 m. This structure had been previously tested physically (Candeias et al. 2017) and numerically (Mendes et al. 2017, AlShawa et al. 2017).

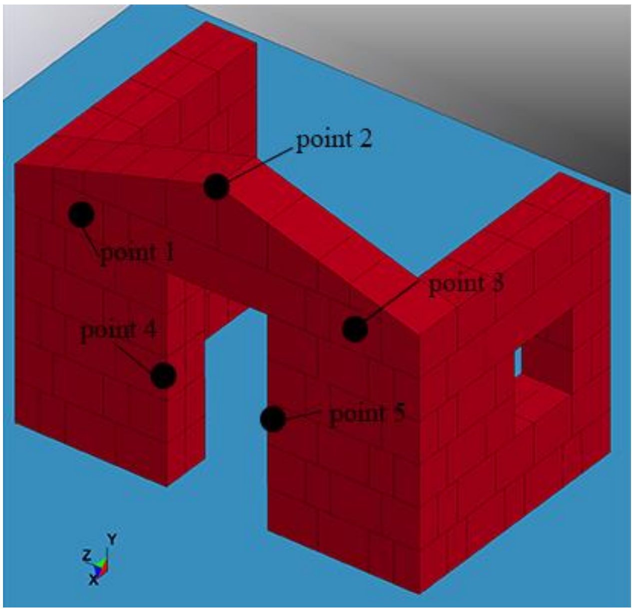

Figure 7. Masonry test structure.

The test structure was modelled by means of a combined finite-discrete element strategy implemented in LS-DYNA (Hallquist 2006). The model has discrete components, i.e. block elements and contact interfaces. The three-dimensional model was able to capture the experimentally observed mechanisms, without any *a priori* assumption about the mechanism itself.

The modelling approach for the block elements allows for cracking, separation, and re-contact along predefined contact surfaces. In order to avoid significant bias in the failure mechanism, the interfaces must be plentiful, and at the same time must be limited in number to contain modelling and computational burden. Consequently, a block element represents several masonry units and mortar joints. Linear-elastic behaviour is assumed for the material. Young's modulus, E, and density, ρ, of the units have been set at: E = 2077 MPa, ρ = 2360 kg/m^3. Poisson's ratio has been set at 0.2. Damping ratio has been assumed to be 0.05. The standard unit in the model is 500 × 250 × 400 mm^3. The blocks are parallelepipeds, more regular than the real ones. The number of blocks and of FE total 169 and 7716, respectively (AlShawa et al. 2017).

Regarding contact interfaces, automatic detection of contact is implemented. Explicit time integration is adopted, providing more stable results when contact interfaces are present (Burnett et al. 2007, Jäger et al. 2009, Srewil 2008). Interfaces transmit both compression and tension, with optional failure criteria for the latter (Bala 2007). Tension is resisted by a linear contact spring until failure. Spring failure criterion is based on normal force alone, that is, the spring is removed when:

$$\sigma_n \geq NFLS \tag{18}$$

where σ_n is the normal stress on the contact surface and *NFLS* the normal (tensile) failure limit stress. Post-failure interaction takes place according to classical compression-friction contact. Initiation of sliding is controlled by shear failure limit stress in the absence of normal stress, *SFLS*, representing the interface cohesion, and by friction, governed by Coulomb's law. The analyses assume *SFLS* = *NFLS*, based on a pure shear condition (Calderini et al. 2010), where *SFLS* = *NFLS* = 0.010, 0.150 MPa (AlShawa et al. 2017), the lower value accounting for smooth units and decayed mortar, as commonly found in many buildings damaged/collapsed following the Amatrice-Norcia earthquake. Once shear capacity has been exceeded, sliding is controlled by static and dynamic friction coefficients. For both static and dynamic friction coefficients, values μ = 0.4, 0.6, 0.8 have been adopted, based on experimental values reported in Burnett et al. (2007), Maheri et al. (2011), Liberatore et al. (2016), the lowest value representing the masonry characteristics of many buildings involved in the Amatrice-Norcia earthquake. The dynamic friction coefficient has been assumed to be equal to the static coefficient because of lack of experimental data on the types of masonry investigated.

The out-of-plane displacement time histories of point 2 (Figure 7) under CLO record of 30th October 2016 (see Table 3), which is associated with the maximum downward displacement (w = –0.780 m), are shown in Figures 8 and 9. Either the NS or EW component was applied along the direction orthogonal to the façade. The vertical component is assumed to be either acting or not.

It can be noticed that the vertical component produces displacement shifts in some time histories for *SFLS* = *NFLS* = 0.010 MPa (μ = 0.4, EW; μ = 0.6, NS; μ = 0.8, EW), indicating an increase in sliding at unit-mortar interfaces (Figure 8).

The minimum (negative, inwards) and maximum (positive, outwards) values of displacement at points 1-5 and base shear are reported in Figures 10-13. Displacements in absolute value greater than 200 mm are associated with large out-of-plumb, corresponding to failure – or near failure – condition of the wall. It can be noticed that a number of failures occur for *SFLS* = *NFLS* = 0.010 MPa, consistent with the post-earthquake reconnaissance of damage. No failures occur for *SFLS* = *NFLS* = 0.150 MPa. Increases in base shear can be observed for *SFLS* = *NFLS* = 0.150 MPa compared to *SFLS* = *NFLS* = 0.150 MPa.

It can be noticed that response under the NS component is generally higher than that under the EW component, in terms of both displacements and base shear, consistent with the corresponding response spectra (Luzi et al. 2017).

The vertical component induces a set of additional failures for *SFLS* = *NFLS* = 0.010 MPa, namely: $\mu = 0.4$, NS (points 4, 5), EW (point 3); $\mu = 0.8$, EW (point 3), and base shear shows a mean increment of 9%. On the other hand, for *SFLS* = *NFLS* = 0.150 MPa, the effect of the vertical component is generally limited, with a mean relative decrement of 3% in displacements and an increment of 1% in base shear. These limited effects can be explained on the basis of the frequency content of the vertical ground acceleration, greater in the high frequency range, compared to displacement along horizontal directions. During a single sliding along a mortar joint, several cycles of normal (vertical) stress occur, along with a corresponding increase/decrease of friction force, resulting in a non-systematic effect on the total sliding.

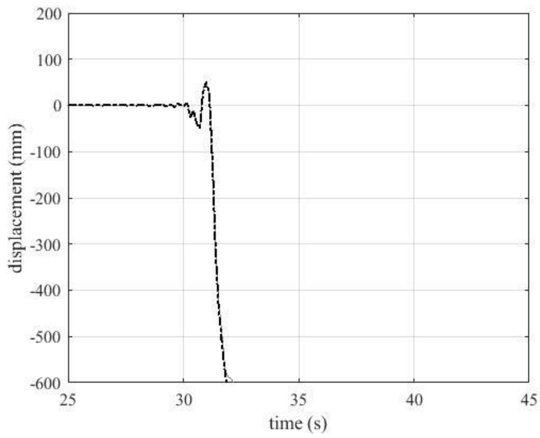

a) NS, $\mu = 0.4$

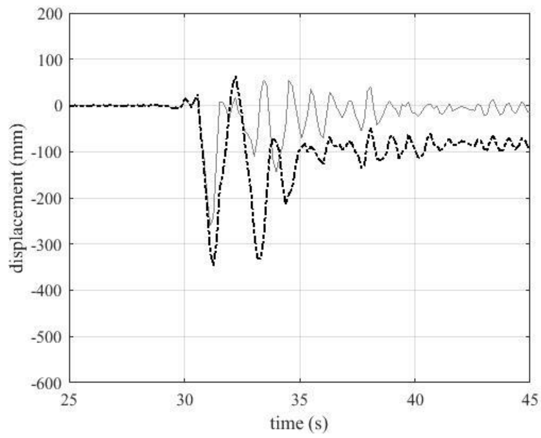

b) EW, $\mu = 0.4$

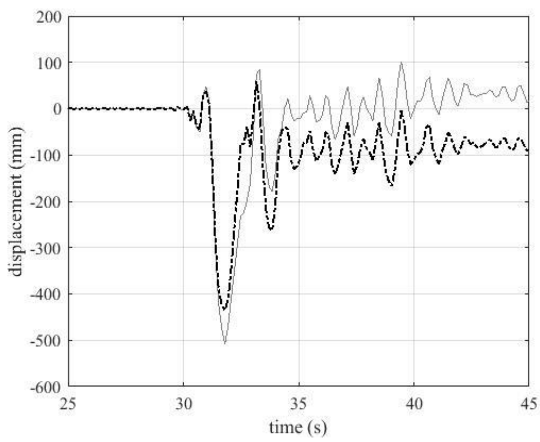

c) NS, $\mu = 0.6$

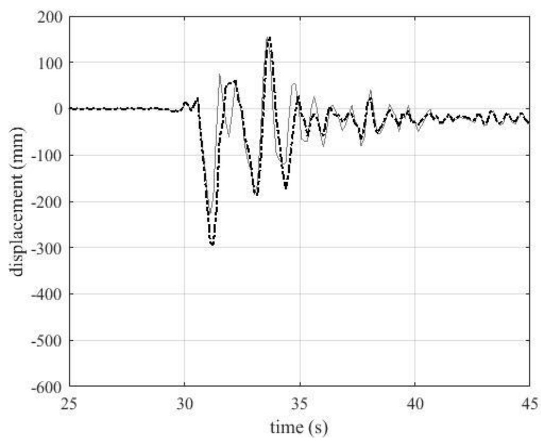

d) EW, $\mu = 0.6$

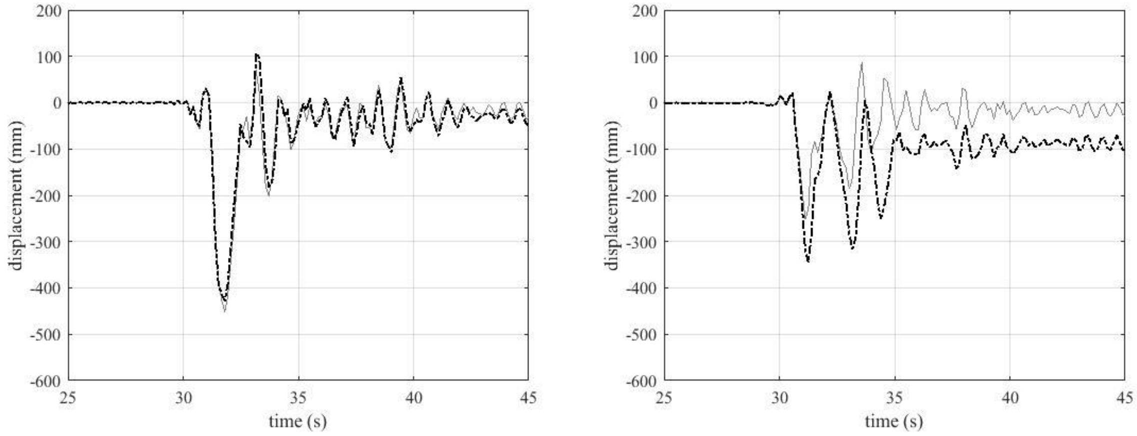

e) NS, $\mu = 0.8$ *f)* EW, $\mu = 0.8$

Figure. 8. Out-of-plane displacement time histories of point 2 of the test structure subjected to the CLO record of 30th October 2016, *SFLS* = *NFLS* = 0.010 MPa (grey: without the vertical component; black: with the vertical component).

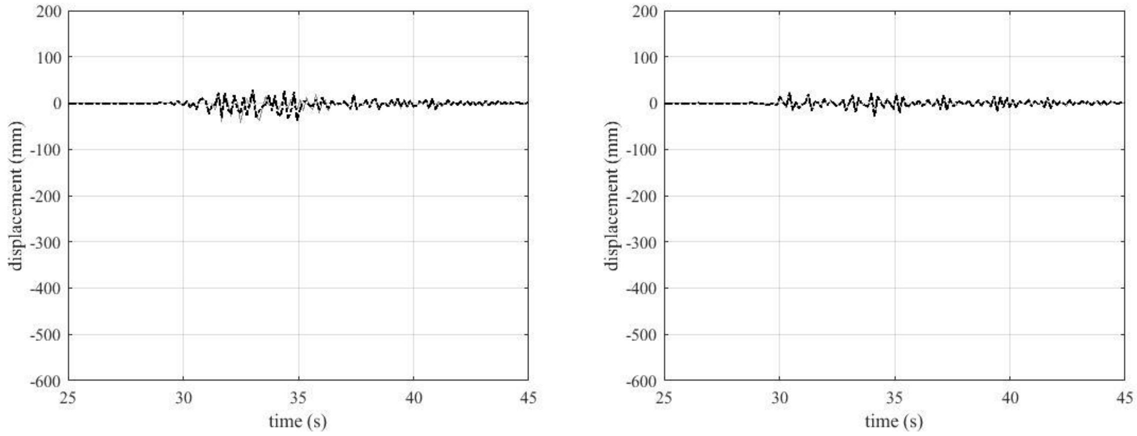

a) NS, $\mu = 0.4$ *b)* EW, $\mu = 0.4$

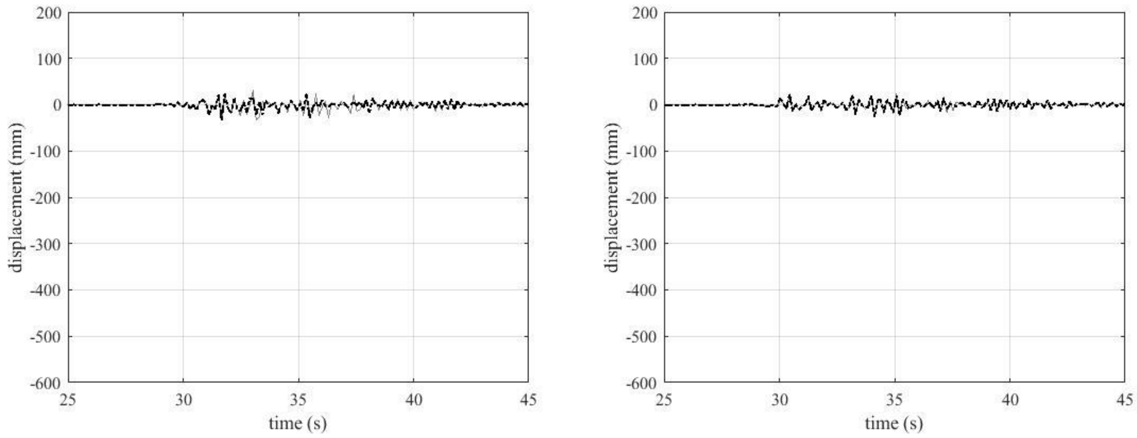

c) NS, $\mu = 0.6$ *d)* EW, $\mu = 0.6$

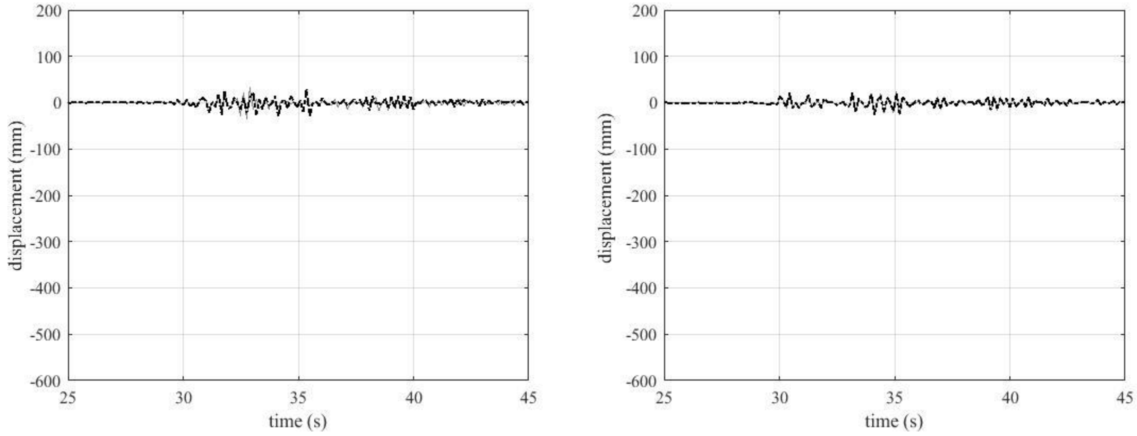

e) NS, $\mu = 0.8$ *f)* EW, $\mu = 0.8$

Figure. 9. Out-of-plane displacement time histories of point 2 of the test structure subjected to the CLO record of 30th October 2016, *SFLS* = *NFLS* = 0.150 MPa (grey: without the vertical component; black: with the vertical component).

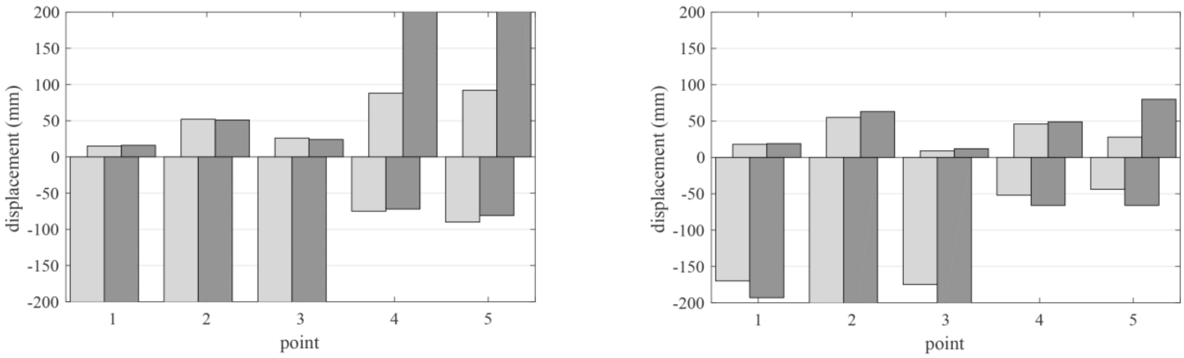

a) NS, $\mu = 0.4$ *b)* EW, $\mu = 0.4$

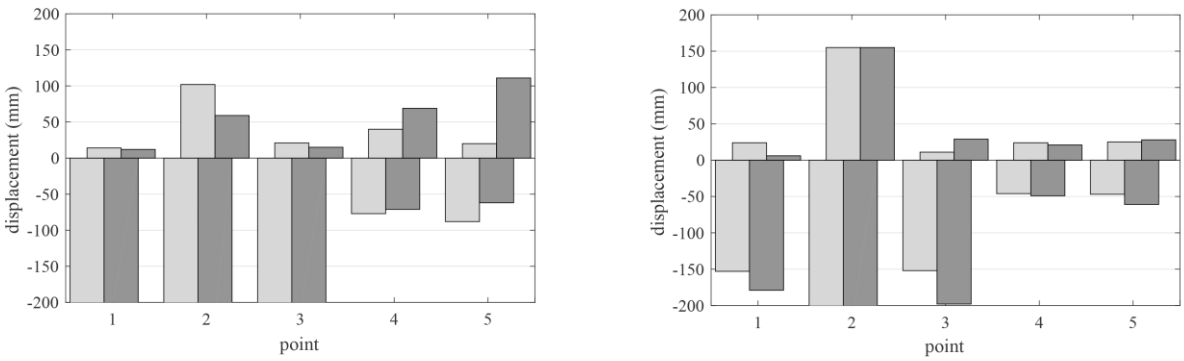

c) NS, $\mu = 0.6$ *d)* EW, $\mu = 0.6$

This is a post-peer-review, pre-copyedit version of an article published in Soil Dynamics and Earthquake Engineering. The final authenticated version is available online at: http://dx.doi.org/10.1016/j.soildyn.2019.02.015

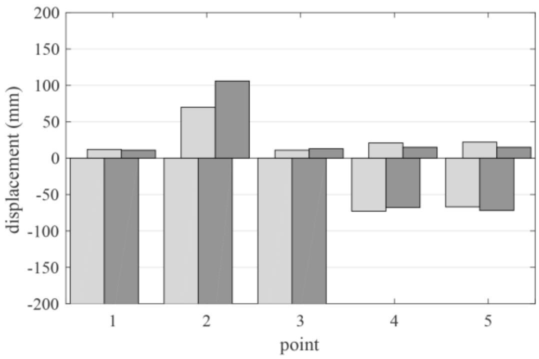

e) NS, $\mu = 0.8$

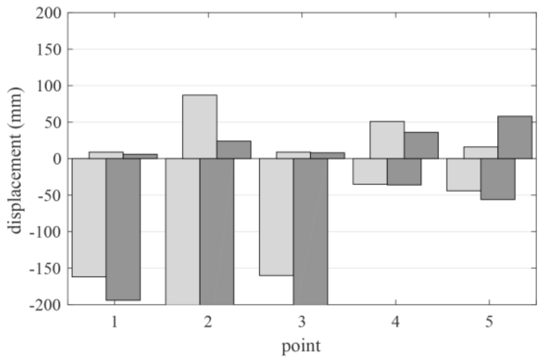

f) EW, $\mu = 0.8$

Figure 10. Minimum/maximum displacements of the test structure subjected to the CLO record of 30th October 2016, *SFLS* = *NFLS* = 0.010 MPa (light grey: without the vertical component; dark grey: with the vertical component).

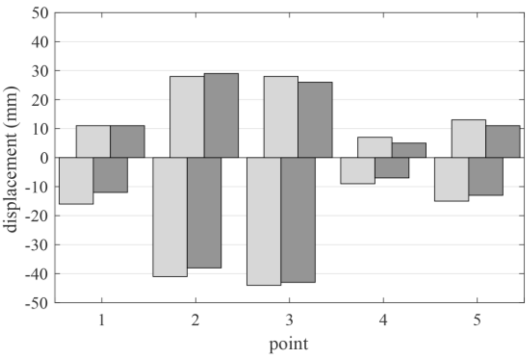

a) NS, $\mu = 0.4$

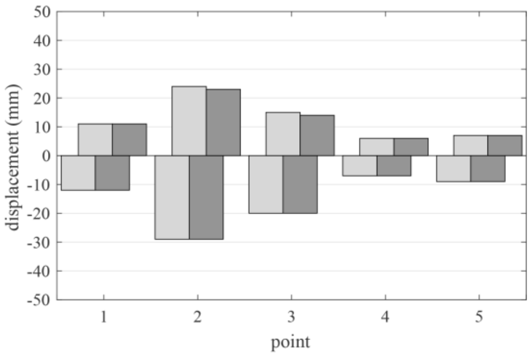

b) EW, $\mu = 0.4$

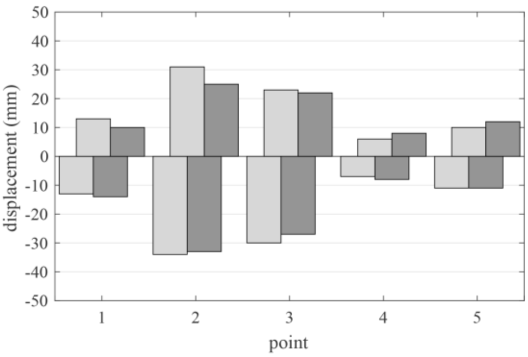

c) NS, $\mu = 0.6$

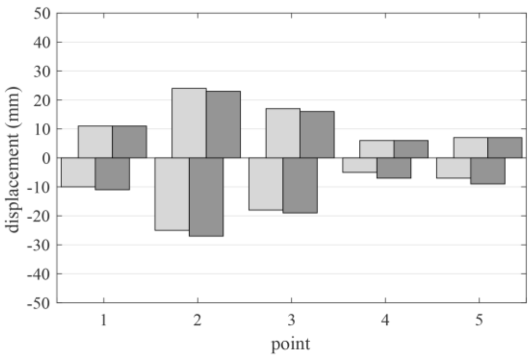

d) EW, $\mu = 0.6$

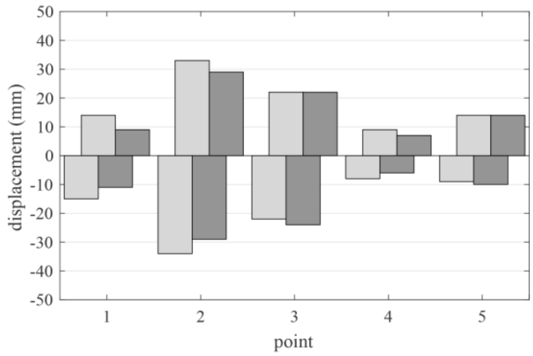

e) NS, $\mu = 0.8$

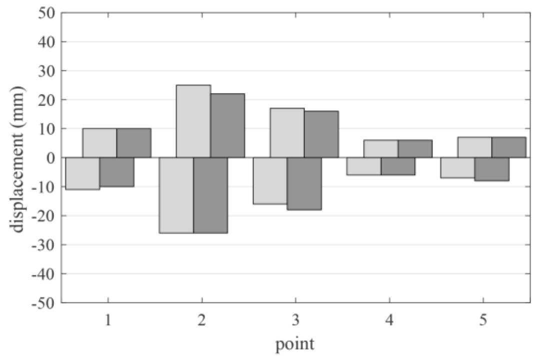

f) EW, $\mu = 0.8$

Figure 11. Minimum/maximum displacements of the test structure subjected to the CLO record of 30th October 2016, *SFLS* = *NFLS* = 0.150 MPa (light grey: without the vertical component; dark grey: with the vertical component).

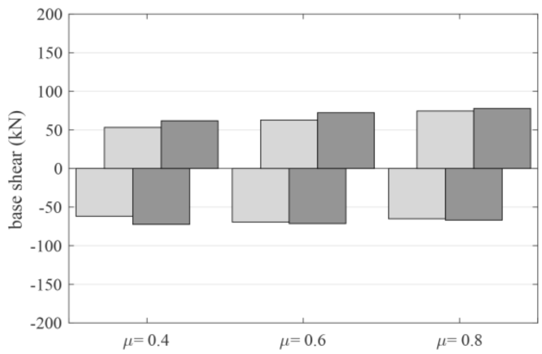

a) NS

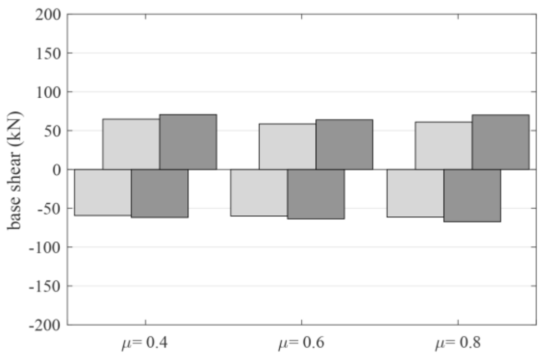

b) EW

Figure 12. Minimum/maximum base shear of the test structure subjected to the CLO record of 30th October 2016, *SFLS* = *NFLS* = 0.010 MPa (light grey: without the vertical component; dark grey: with the vertical component).

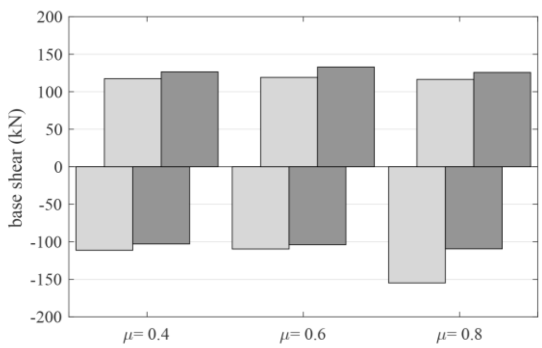

a) NS

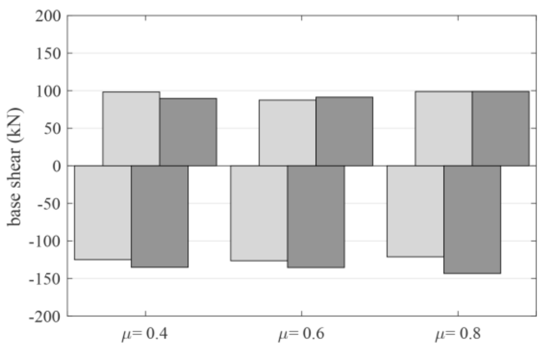

b) EW

Figure 13. Minimum/maximum base shear of the test structure subjected to the CLO record of 30th October 2016, *SFLS* = *NFLS* = 0.150 MPa (light grey: without the vertical component; dark grey: with the vertical component).

6 CONCLUSIONS

This paper presents an analysis of InSAR data for the 2016 Amatrice-Norcia earthquake. The research stemed from the observation that the most severe damage is localized in the area that underwent subsidence, whereas zones closer to the epicentre, but coseismically uplifted, experienced less destruction. This observation is confirmed by statistical analyses, showing good correlation between InSAR downward displacement and macroseismic intensity.

The effect of vertical acceleration, and the ensuing variation of friction forces between units and mortar in a masonry building, is investigated by means of numerical simulations on a test structure with cohesive-frictional unit-mortar interface. The test structure was subjected to the horizontal component only, and to the horizontal component combined with the vertical component. The vertical component induces more extensive failures in structures with small cohesion, whereas it has limited effects in structures with medium cohesion. This behaviour can be ascribed to the greater high-frequency content of vertical ground acceleration, compared to horizontal displacement. During a single sliding along a mortar joint, several cycles of normal (vertical) stress occur at the interface, with increasing/decreasing friction force, resulting in non-systematic effects on the total sliding. However, during the time intervals when friction is lower, larger sliding occurs, with greater masonry damage.

The correlation between InSAR displacement and damage can be explained on the basis of ground motion intensity measures. In fact, statistical analyses showed good correlation between InSAR vertical displacement on the one hand, and the ratio *PGA*/*PGV* and Housner Intensity on the other. Housner Intensity, in particular, has been proved by literature studies to be well correlated to macroseismic intensity and structural damage.

Future developments of this study will investigate the relationships of macroseismic intensity and ground motion intensity measures vs. InSAR vertical displacement for earthquakes with different characteristics, in particular reverse focal mechanism and upward displacement in the epicentral zone.

ACKNOWLEDGEMENTS

The authors are grateful to Francesco Doglioni for fruitful discussions and Andrea Tertulliani for providing the location of macroseismic data for the 2016 seismic sequence.

REFERENCES

AlShawa O, Sorrentino L, Liberatore D (2017) Simulation of Shake Table Tests on Out-of-Plane Masonry Buildings. Part (II): Combined Finite-Discrete Elements. Int J Archit Herit 11(1):79-93. https://doi.org/10.1080/15583058.2016.1237588

Anderson JC, Bertero VV (1987) Uncertainties in establishing design earthquakes. J Struct Eng 113(8):1709-1724. https://doi.org/10.1061/(ASCE)0733-9445(1987)113:8(1709)

Arias A (1970) A measure of earthquake intensity. In: Hansen RJ (ed) Seismic Design for Nuclear Power Plants, 438-483.

Atzori S, Hunstad I, Chini M, Salvi S, Tolomei C, Bignami C, Stramondo S, Trasatti E, Antonioli A, Boschi E (2009) Finite fault inversion of DInSAR coseismic displacement of the 2009 L'Aquila earthquake (Central Italy), Geoph. Res. Lett., 36, L15305. https://doi.org/10.1029/2009GL039293

Azzaro R, Tertulliani A, Bernardini F, Camassi R, Del Mese S, Ercolani E, Graziani L, Locati M, Maramai A, Pessina V, Rossi A, Rovida A, Albini P, Arcoraci L, Berardi M, Bignami C, Brizuela B, Castellano C, Castelli V, D'Amico S, D'Amico V, Fodarella A, Leschiutta I, Piscini A, Sbarra M (2016) The 24 August 2016 Amatrice earthquake: macroseismic survey in the damage area and EMS intensity assessment. Annals of Geophysics, 59, Fast Track 5. https://doi.org/10.4401/ag-7203

Bala S (2007) Tie-Break Contacts in LS-DYNA. Livermore, CA: Livermore Software.

Bigi G, Castellarin A, Catalano R, Coli M, Cosentino D, Dal Piaz GV, Lentini F, Parotto M, Patacca E, Praturlon A, Salvini F, Sartori R, Scandone P, Vai GB (1989) Synthetic structural-kinematic map of Italy , scale 1:2.000.000. CNR, Progetto Finalizzato Geodinamica, Roma.

Burnett S, Gilbert M, Molyneaux T, Beattie G, Hobbs B (2007) The performance of unreinforced masonry walls subjected to low-velocity impacts: Finite element analysis. International Journal of Impact Engineering 34(8):1433-50. https://doi.org/10.1016/j.ijimpeng.2006.08.004

Cabañas L, Benito B, Herráiz M (1997) An approach to the measurement of the potential structural damage of earthquake ground motions. Earthq Eng Struct Dyn 26:79-92.

https://doi.org/10.1002/(SICI)1096-9845(199701)26:1<79::AID-EQE624>3.0.CO;2-Y

Calderini C, Cattari S, Lagomarsino S (2010) The use of the diagonal compression test to identify the shear mechanical parameters of masonry. Construction and Building Materials 24:677-85. https://doi.org/10.1016/j.conbuildmat.2009.11.001

Calderoni G, Rovelli A, Di Giovambattista R (2017) Rupture directivity of the strongest 2016-2017 Central Italy earthquakes. Journal of Geophysical Research: Solid Earth. 122(11):9118-9131. https://doi.org/10.1002/2017JB014118

Candeias PX, Campos Costa A, Mendes N, Costa AA, Lourenço PB (2017) Experimental assessment of the out of plane performance of masonry buildings through shake table tests. Int J Archit Herit 11(1):79-93. https://doi.org/10.1080/15583058.2016.1238975

Castaldo P, Tubaldi E (2018) Influence of ground motion characteristics on the optimal single concave sliding bearing properties for base-isolated structures. Soil Dynamics and Earthquake Engineering 104:346-364. http://dx.doi.org/10.1016/j.soildyn.2017.09.025

Cheloni D, De Novellis V, Albano M, Antonioli A, Anzidei M, Atzori S, Avallone A, Bignami C, Bonano M, Calcaterra S, Castaldo R, Casu F, Cecere G, De Luca C, Devoti R, Di Bucci D, Esposito A, Galvani A, Gambino P, Giuliani R, Lanari R, Manunta M, Manzo M, Mattone M, Montuori A, Pepe A, Pepe S, Pezzo G, Pietrantonio G, Polcari M, Riguzzi F, Salvi S, Sepe V, Serpelloni E, Solaro G, Stramondo S, Tizzani P, Tolomei C, Trasatti E, Valerio E, Zinno I, Doglioni C (2017) Geodetic model of the 2016 Central Italy earthquake sequence inferred from InSAR and GPS data, Geoph. Res. Lett. 44:6778-6787. https://doi.org/10.1002/2017GL073580

Chiaraluce L, Di Stefano R, Tinti E, Scognamiglio L, Michele M, Casarotti E, Cattaneo M, De Gori P, Chiarabba C, Monachesi G, Lombardi A, Valoroso L, Latorre D, Marzorati S (2017) The 2016 Central Italy seismic sequence: A first look at the mainshocks, aftershocks, and source models. Seismological Research Letters 88(3):757-771. https://doi.org/10.1785/0220160221

Chiauzzi L, Masi A, Mucciarelli M, Vona M, Pacor F, Cultrera G, Gallovič F, Emolo A (2012) Building damage scenarios based on exploitation of Housner intensity derived from finite faults ground motion simulations. Bull Earthq Eng 10:517-545. https://doi.org/10.1007/s10518-011-9309-8

Decanini L, Mollaioli F, Oliveto G (2002) Structural and seismological implications of the 1997 seismic sequence in Umbria and Marche, Italy. In: Oliveto G (ed) Innovative approaches to earthquake engineering, 229-323. WIT Press, Southampton, United Kingdom.

Devoti R, D'Agostino N, Serpelloni E, Pietrantonio G, Riguzzi F, Avallone A, Cavaliere A, Cheloni D, Cecere G, D'Ambrosio C, Falco L, Selvaggi G, Métois M, Esposito A, Sepe V, Galvani A, Anzidei M (2017) A combined velocity field of the Mediterranean region. Annals of

Geophysics, 60(2), S0217. https://doi.org/10.4401/ag-7059

Doglioni C, Carminati E, Petricca P, Riguzzi F (2015) Normal fault earthquakes or graviquakes. Scientific reports, 5, 12110. https://doi.org/10.1038/srep12110

Fajfar P, Vidic T, Fischinger M (1990) A measure of earthquake motion capacity to damage medium-period structures. Soil Dyn Earthq Eng 9(5):236-242. https://doi.org/10.1016/S0267-7261(05)80002-8

Franceschetti G, Lanari R (1999) Synthetic Aperture Radar Processing, CRC Press, Boca Raton (FL), ISBN 8493-7899.

Galli P, Peronace E, Bramerini F, Castenetto S, Naso G, Cassone F, Pallone F (2016) The MCS intensity distribution of the devastating 24 August 2016 earthquake in central Italy (M_w 6.2). Annals of Geophysics 59, Fast Track 5. https://doi.org/10.4401/ag-7287

Galvani A, Anzidei M, Devoti R, Esposito A, Pietrantonio G, Pisani AR, Riguzzi F, Serpelloni E (2012) The interseismic velocity field of the central Apennines from a dense GPS network. Ann. Geophys. 55(4). https://doi.org/10.4401/ag-6168

Ganz M, Doglioni F (2014) Criteri per il riconoscimento dell’origine sismica di danni stratificati. Il Santuario dei SS. Vittore e Corona a Feltre come tema di Archeosismologia. Archeologia dell’Architettura, XIX.

Hallquist JO (2006) LS-DYNA *Theory Manual*. Livermore, CA: Livermore Software Technology Corporation.

Housner GW (1952) Spectrum Intensities of Strong Motion Earthquakes. In: Proceedings of the Symposium of Earthquake and Blast Effects on Structures, EERI, Los Angeles, California, 21-36.

Jäger W, Bakeer T, Schöps P (2009) Simulation of Masonry in ANSYS and LS-DYNA The Features and Challenges. ANSYS Conference & 27th CADFEM Users’ Meeting 2009, November 18-20, 2009 Congress Center Leipzig, Germany.

Liberatore D, Masini N, Sorrentino L, Racina V, Sileo M, AlShawa O, Frezza L (2016) Static penetration test for historical masonry mortar. Construction and Building Materials 122:810-822. https://doi.org/10.1016/j.conbuildmat.2016.07.097

Luzi L, Pacor F, Puglia R (2017) Italian Accelerometric Archive v. 2.3. Istituto Nazionale di Geofisica e Vulcanologia, Dipartimento della Protezione Civile Nazionale. https://doi.org/10.13127/ITACA.2.3

Margottini C, Molin D, Narcisi B, Serva L (1987) Intensity vs. acceleration: Italian data. Proceedings of the Workshop on Historical Seismicity of Central-Eastern Mediterranean Region. ENEA-IAEA, Roma, 213-226.

Mariani M, Pugi F (2018) Effetti negativi del sisma verticale sul comportamento delle pareti esistenti in muratura. Ingenio, 25/07/2018.

Marotta A, Sorrentino L, Liberatore D, Ingham JM (2018) Seismic risk assessment of New Zealand unreinforced masonry churches using statistical procedures. Int J Archit Herit 12(3):448-464. https://doi.org/10.1080/15583058.2017.1323242

Masi A, Chiauzzi L, Braga F, Mucciarelli M, Vona M, Ditommaso R (2011) Peak and integral seismic parameters of L’Aquila 2009 ground motions: Observed versus code provision values. Bull Earthq Eng 9:139-156. https://doi.org/10.1007/s10518-010-9227-1

Mendes N, Costa AA, Lourenço PB, Bento R, Beyer K, de Felice G, Gams M, Griffith MC, Ingham JM, Lagomarsino S, Lemos JV, Liberatore D, Modena C, Oliveira DV, Penna A, Sorrentino L (2017) Methods and Approaches for Blind Test Predictions of Out-of-Plane Behavior of Masonry Walls: A Numerical Comparative Study. Int J Archit Herit 11(1):59-71. https://doi.org/10.1080/15583058.2016.1238974

Petricca P, Barba S, Carminati E, Doglioni C, Riguzzi F (2015) Graviquakes in Italy. Tectonophysics 656(12):202-2014. https://doi.org/10.1016/j.tecto.2015.07.001

Sorrentino L, Cattari S, da Porto F, Magenes G, Penna A (2018) Seismic behaviour of ordinary masonry buildings during the 2016 Central Italy Earthquakes. Bull Earthq Eng. https://doi.org/10.1007/s10518-018-0370-4

Srewil Y (2008) Risk studies for squatter settlements of big cities: A case example of earthquakes at Damascus. Master thesis, Dresden University of Technology, Dresden, Germany.

Stafford PJ, Berrill JB, Pettinga, JR (2009) New predictive equations for Arias intensity from crustal earthquakes in New Zealand. Journal of Seismology 13:31-52. https://doi.org/10.1007/s10950-008-9114-2

Tertulliani A, Azzaro R (eds) (2016) QUEST - Rilievo macrosismico per i terremoti nell’Italia centrale. Aggiornamento dopo le scosse del 26 e 30 ottobre 2016, rapporto interno INGV, Roma. https://doi.org/10.5281/zenodo.182694

Trifunac MD, Brady AG (1975) A study on the duration of strong earthquake ground motion. Bull Seismol Soc Am 65:581-626. https://doi.org/10.1016/0148-9062(76)90487-3

Uang C, Bertero V (1988) Implications of recorded earthquake ground motions on seismic design of building structures UCB/EERC-88/13. Rep. n. UCB/EERC-88/13.

Weston J, Ferreira AMG, Funning GJ (2011) Global compilation of interferometric synthetic aperture radar earthquake source models: 1. Comparisons with seismic catalogs. J. Geophys. Res., 116, B08408. https://doi.org/10.1029/2010JB008131

Wilkinson MW, McCaffrey KJW, Jones RR, Roberts GP, Holdsworth RE, Gregory LC, Walters

RJ, Wedmore L, Goodall H, Iezzi F (2017) Near-field fault slip of the 2016 Vettore M_w 6.6 earthquake (Central Italy) measured using low-cost GNSS. Scientific Reports 7:4612. https://doi.org/10.1038/s41598-017-04917-w